Sensitivity of the Simulated Climate to a Diagnostic Formulation for Cloud Liquid Water

JAMES J. HACK

National Center for Atmospheric Research, Boulder, Colorado*

(Manuscript received 14 April 1997, in final form 8 August 1997)

ABSTRACT

The accurate treatment of clouds and their radiative properties is widely regarded to be among the most important problems facing global climate modeling. A number of the more serious systematic simulation biases in the NCAR Community Climate Model (CCM2) appear to be related to deficiencies in the treatment of cloud optical properties. In this paper, a simple diagnostic parameterization for cloud liquid water is presented. The sensitivity of the simulated climate to this alternative formulation, both in terms of mean climate metrics and measures of the climate system response, is illustrated. Resulting simulations show significant reductions in CCM2 systematic biases, particularly with respect to surface temperature, precipitation, and extratropical geopotential height-field anomalies. Many aspects of the simulated response to ENSO forcing are also substantially improved.

1. Introduction

It is widely recognized that clouds exert an important forcing on the climate system, as regulators of the radiative heating field and more directly through vertical energy transports, where each of these forcing phenomena take place on very small scales of motion. Our relatively poor understanding of cloud processes, and their effect on the distribution of diabatic heating in the atmosphere, continues to pace efforts to better simulate the general circulation and represents one of the principal sources of uncertainty in the modeling and prediction of global climate (e.g., Cess et al. 1990).

How to generate a cloud distribution in large-scale numerical models and properly represent the associated radiative properties remains an unresolved problem. Convergence toward a common methodology is most severely limited by a lack of observational knowledge about the large-scale interaction of clouds with the radiation field. The global modeling community is generally limited to validating cloud parameterizations on the basis of their top-of-atmosphere (TOA) radiative characteristics only (e.g., high quality global surface radiation datasets based on direct measurements are nonexistant), which provide important but incomplete constraints on evaluating the performance of competing parametric techniques. Consequently, there are a wide range of approaches to the parameterization of clouds and their radiative effects in large-scale atmospheric models. Early global models prescribed both the cloud distribution and their optical properties (e.g., Smagorinsky et al. 1965). Diagnostic techniques for determining the formation and dissipation of cloud as a function of the atmospheric state followed (e.g., Slingo 1987), where the cloud radiative properties were either prescribed in very simple ways (e.g., Ramanathan et al. 1983) or were determined on the basis of moist thermodynamic arguments (e.g., Sommerville and Remer 1984; Betts and Harshvardhan 1987). More recently, the global modeling community has been vigorously exploring prognostic techniques for describing the cloud field in which bulk microphysical equations are introduced to more explicitly represent the processes responsible for the formation, transport, and dissipation of cloud water and cloud ice (e.g., Sundqvist 1988; Smith 1990; Tiedke 1993; Sundqvist 1993; Fowler et al. 1996; Del Genio et al. 1996). The advantage of this latter class of parameterizations is that, in principle, they should provide more realistic representations of the cloud field. The disadvantages are the introduction of a large number of new free parameters (which are difficult to validate on general circulation scales of motion) and additional computational expense.

One example of the importance of properly describing the interaction of the cloud field with the radiation field can be seen in the simulation of the NCAR Community Climate Model, version 2 (CCM2). The formulation of the CCM2 (Hack et al. 1993) represented a significant departure from earlier versions of this model, where

* The National Center for Atmospheric Research is sponsored by the National Science Foundation.

Corresponding author address: Dr. James J. Hack, NCAR/CGD, P.O. Box 3000, Boulder, CO 80307-3000.
E-mail: jhack@ncar.ucar.edu

many of the numerical and physical parameterization components were replaced with considerably more sophisticated methods for treating key climate processes. Many aspects of the CCM2 simulation have been shown to be significantly more realistic when compared with earlier models (e.g., Hack et al. 1994; Kiehl et al. 1994; Hurrell et al. 1993), but a number of important systematic deficiencies remain. Some of these systematic biases would be particularly problematical if the CCM2 were to be coupled to land, ice, and ocean component models. Among the more significant biases are a substantial warm anomaly in simulated July surface temperature over most of the Northern Hemisphere; a systematic overprediction of precipitation maxima, primarily over warm land areas; and excessive ridging over the North Pacific coupled with an anomalous reduction in the height field over western North America during January. Additionally, the implied meridional ocean heat transport in the Southern Hemisphere is in the wrong direction (Kiehl et al. 1998). A principal source of many of these simulation deficiencies has been traced to the CCM2 treatment of cloud optical properties, in this case cloud liquid water path and cloud drop effective radius.

In this paper, we will present a simple diagnostic parameterization for cloud liquid water which will be incorporated in the NCAR Community Climate Model, version 2 (CCM2). We will explore the sensitivity of the simulated climate to this scheme, both in terms of mean climate metrics and measures of the climate system response. We will show that the introduction of this scheme, along with an alternative treatment for the cloud drop effective radius (Kiehl 1994), results in a reduction of many of the CCM2 systematic errors. We illustrate improvements in the simulation, both regionally and globally, and discuss the physical reasons for the response. Because of the clear simulation advantages, these combined formulations for the diagnosis of cloud optical properties form the basis for the cloud parameterization employed in the NCAR CCM3 (see Kiehl et al. 1996).

2. Cloud parameterization in the NCAR CCM2

Existing cloud parameterization schemes belong to one of two classes: diagnostic or statistical schemes, for which cloud properties are parametrically derived from large-scale state information, and prognostic schemes, which introduce additional large-scale state variables to characterize the cloud field. The CCM2 cloud parameterization scheme is among the simpler of diagnostic approaches. Cloud amount (or cloud fraction) is evaluated diagnostically, and the associated cloud optical properties are, for practical purposes, specified. The cloud fraction parameterization amounts to a generalization of the scheme introduced by Slingo (1987) and depends on relative humidity, vertical velocity, atmospheric stability, and the convective precipitation rate (i.e., precipitation arising from the parameterization of moist convection). Three types of cloud are diagnosed by the scheme: convective cloud, layered cloud, and low-level marine stratus. Some of the major changes from Slingo (1987) are clouds are allowed to form in any tropospheric layer except the layer nearest the surface; the minimum convective cloud fraction is 20% (i.e., for nonprecipitating cases); low-level frontal clouds occur for all $\omega < 0$; and the relative humidity thresholds for mid- and upper-level layered clouds are functions of atmospheric stability.

Total column convective cloud amount between the base and top of moist convective activity is diagnosed on the basis of the convective precipitation rate using

$$\overline{A}_{\text{conv}} = 0.20 + 0.125 \ln(1.0 + P), \tag{1}$$

where P is the convective precipitation rate in mm day^{-1} and $\overline{A}_{\text{conv}}$ is not allowed to exceed 80%. The convective cloud amount in each layer is assumed to be randomly overlapped:

$$A_{\text{conv}} = 1.0 - (1.0 - \overline{A}_{\text{conv}})^{1/N}, \tag{2}$$

where N is the number of model levels within the convectively active region. The large-scale relative humidity within the grid box is then adjusted to account for the assumption that the fractional area of convective cloud, A_{conv}, is saturated. This adjusted large-scale relative humidity, RH′, is given by

$$\text{RH}' = \frac{\text{RH} - A_{\text{conv}}}{1 - A_{\text{conv}}}, \tag{3}$$

where RH is the true grid-box relative humidity.

Frontal and tropical low-cloud fraction, that is, clouds occurring below 750 mb, is diagnosed using

$$A_c = \left(\frac{\text{RH}' - 0.9}{0.1}\right)^2 \qquad \omega < 0, \tag{4}$$

while stratus associated with low-level inversions is determined from

[see Eq. (5) on next page],

where $\partial\theta/\partial p$ is the maximum inversion strength. Mid- and high-level stratified (or layered) cloud amount is determined from the relation

$$A_c = \left[\max\left(0, \frac{\text{RH}' - \text{RH}_{\text{lim}}}{1 - \text{RH}_{\text{lim}}}\right)\right]^2, \tag{6}$$

where

$$\text{RH}_{\text{lim}}(p, \phi) = 0.999 - 0.10\left[1 - \frac{N^2}{2.5 \times 10^{-4}}\right]. \tag{7}$$

The quantity N^2 is the square of the Brunt–Väisällä frequency:

$$N^2 = -\frac{g^2\rho}{\theta}\frac{\partial\theta}{\partial p}, \tag{8}$$

$$A_c = \begin{cases} 0 & \mathrm{RH}' < 0.6 \\ \left(-6.67\dfrac{\partial\theta}{\partial p} - 0.667\right) \times \left(1 - \dfrac{0.9 - \mathrm{RH}'}{0.3}\right) \times \left(\dfrac{P - 750}{150}\right) & 0.6 \le \mathrm{RH}' \le 0.9 \quad \text{and} \quad \dfrac{\partial\theta}{\partial p} < -0.125,\ 750 \le p \le 900 \\ \left(-6.67\dfrac{\partial\theta}{\partial p} - 0.667\right) \times \left(\dfrac{P - 750}{150}\right) & \mathrm{RH}' > 0.9 \quad \text{and} \quad \dfrac{\partial\theta}{\partial p} < -0.125, \end{cases} \tag{5}$$

where the ratio $N^2/2.5 \times 10^{-4}$ is not allowed to exceed 1. The total cloud fraction in any layer is defined as

$$A_c = (1.0 - A_{\mathrm{conv}})\, A_c + A_{\mathrm{conv}}. \tag{9}$$

The longwave radiative parameterization in CCM2 employs the broadband technique described in Kiehl et al. (1987) and incorporates a Voigt line shape to more accurately treat infrared radiative cooling in the stratosphere (Kiehl and Briegleb 1991). Solar absorption is calculated with a δ-Eddington approximation using 18 spectral intervals (Briegleb 1992). The diurnal cycle is also represented, where both solar and longwave heating rates are evaluated every hour. For the longwave calculation cloud, emissivity depends entirely on cloud liquid water path. In the solar calculation, cloud optical properties are accounted for using the Slingo (1989) parameterization for liquid water droplet clouds. This scheme relates the extinction optical depth, the single-scattering albedo, and the asymmetry parameter to the cloud liquid water path (LWP) and cloud drop effective radius (r_e), which for extinction optical depth takes the form

$$\tau_{\mathrm{cld}} = \mathrm{LWP}\left(a + \frac{b}{r_e}\right). \tag{10}$$

The two-cloud microphysical parameters, LWP and r_e, are specified quantities in the CCM2, where the CCM2 formalism does not differentiate between water and ice clouds. The cloud drop effective radius is simply set to 10 μm for all clouds. In-cloud liquid water path (what we will also refer to as cloud water path) is evaluated from a prescribed cloud liquid water density profile, $\rho_l(z)$, which is analytically determined on the basis of a specified liquid water scale height (Kiehl et al. 1994):

$$\mathrm{CWP} = \int \rho_l\, dz, \tag{11}$$

where

$$\rho_l = \rho_l^0 e^{(-z/h_l)}, \tag{12}$$

and ρ_l^0 is equal to 0.18 g m^{-3}. The liquid water scale height, h_l, is a time-independent, meridionally varying, empirically derived quantity, which is evaluated using

$$h_l = \mathcal{A} + \mathcal{B}\cos^2\phi, \tag{13}$$

where $\mathcal{A} = 1080$ m and $\mathcal{B} = 2000$ m. The actual grid-area-averaged liquid water path is simply the point-wise product of the in-cloud liquid water path and the cloud fraction

$$\mathrm{LWP} = A_c\mathrm{CWP}. \tag{14}$$

As mentioned earlier, one of the principal weaknesses of the NCAR CCM2 is believed to be the relatively rigid formalism for determining the cloud optical properties. Although the CCM2 cloud parameterization diagnoses the fractional cloud amount in three space dimensions, it specifies the three-dimensional distribution of the in-cloud liquid water concentration, ρ_l. The e-folding rate for the prescribed vertical distribution of ρ_l depends only on the cloud liquid water scale height (specified to be large in the Tropics and small at high latitudes). Thus, h_l uniquely determines the vertical structure for ρ_l and strongly influences the optical properties of the diagnosed cloud field. A physical interpretation of the scale height parameter is easiest to understand by considering the behavior of the cloud scheme in the thermodynamic limit; that is, a saturated column completely filled with cloud. Any increase in the scale height would produce a larger liquid water concentration profile and a correspondingly larger liquid water path. One way to relax the CCM2 framework would be to express this parameter in terms of atmospheric state information that might be related to the formation of cloud condensate.

In this study we explore such a modification where we continue to employ the same exponentially decaying vertical profile for in-cloud liquid water concentration given by (12). Our approach is based on a thermodynamic argument that larger values of water vapor (e.g., in a warmer atmosphere) are associated with larger amounts of cloud condensate [e.g., along the lines of the cloud liquid water feedback arguments in Sommerville and Remer (1984) and Betts and Harshvardhan

(1987)]. Therefore, we use the precipitable water (i.e., the vertically integrated water vapor) predicted by the large-scale model as a vertically integrated measure of the available condensate, and locally relate it to the cloud liquid water scale height h_l using

$$h_l = a \ln\left(1.0 + \frac{b}{g}\int_{p_T}^{p_s} q \, dp\right), \tag{15}$$

where $a = 700$ m and $b = 1$ m^2 kg^{-1} for the purposes of this investigation. The cloud water path for a particular atmospheric layer continues to be determined by integrating the liquid water concentration obtained from (12) using (11). This quantity is then multiplied by the diagnosed cloud amount to produce the actual grid-area-averaged liquid water path (14). Thus, for the same cloud amount A_c (i.e., the same volume occupied by cloud), an atmospheric column with a large precipitable water content will have a larger liquid water path than an atmospheric column with a small precipitable water content. This approach merely extends the CCM2 cloud water framework using a simple empirical thermodynamic argument. It does not address the issue of whether an exponentially decaying profile for in-cloud liquid water concentration is an appropriate approximation. Although the merits of the overall parameterization approach cannot be demonstrated from first principles, they can be evaluated using global sensitivity experiments.

The remainder of this paper will examine the impact of replacing (13) with (15) in several numerical integrations of the CCM2. No modifications to the procedure for diagnosing cloud fraction will be incorporated in these experiments. The majority of the discussion will focus on two numerical experiments which were conducted to illustrate the sensitivity of the CCM2 simulated climate to the revised cloud liquid water parameterization. The first of these experiments (case dlwp0) is a 5-yr simulation using climatological sea surface temperatures. It will be compared to an analogous 20-yr control integration of the CCM2 (case 414). The second experiment (case dlwp0A) is a 5-yr simulation using observed sea surface temperatures for the period 1985–89, which will be compared with a CCM2 control integration for the same period (case 422). Five-year seasonal means for December–February (DJF) and June–August (JJA) will be compared for the climatological SST experiments to illustrate the sensitivity of the mean climate state. The simulations using observed SSTs will be primarily used to examine the model response to ENSO forcing. Throughout the remainder of the manuscript we will refer to the two classes of experiments generically, where DLW will be used to denote diagnostic liquid water experiments, and the CCM2 experiments will also be referred to as control experiments. All numerical experiments include at least a 120-day ''spinup'' period (from a standard CCM2 initial condition), where this adjustment period is excluded from any of the experimental results.

Finally, since observational studies have shown a distinct difference between maritime and continental effective cloud drop size, r_e, Kiehl (1994) explored a scheme for differentiating between the cloud drop effective radius for warm clouds diagnosed over maritime and continental regimes. Over the ocean, the cloud drop effective radius, r_e, is specified to be 10 μm, as in the CCM2. Over landmasses, however, r_e is determined using

$$r_e = \begin{cases} 5\ \mu\text{m} & T > -10^\circ\text{C} \\ 5 - 5\left(\dfrac{T + 10}{20}\right)\ \mu\text{m} & -30^\circ\text{C} \le T \le -10^\circ\text{C} \\ 10\ \mu\text{m} & T < -30^\circ\text{C}. \end{cases} \tag{16}$$

We will briefly examine the climate response to the combination of these two cloud optical property parameterizations using one additional 5-yr experiment forced with observed sea surface temperatures (case dlwp1A) for the period 1985–89.

3. Cloud liquid water characteristics

In this section we examine some of the climatological properties of the diagnosed liquid water field. Global observations of cloud liquid water are a relatively new class of datasets, first appearing in the early 1980s (e.g., Prabhakara et al. 1983; Njoku and Swanson 1983). Microwave radiance techniques have principally been used to retrieve this quantity from satellite, where current retrievals are restricted to estimates of liquid water in the column (i.e., cloud ice is not retrieved), and only over ice-free ocean surfaces (because of highly variable surface emission properties of land surfaces). One additional feature of these satellite-based datasets is that the characteristics of the global distribution appear to strongly depend on specific details of the retrieval algorithm (e.g., Lin and Rossow 1994). Nevertheless, these cloud liquid water estimates do capture many of the more recognizable features of the general circulation (e.g., the ITCZ, extratropical storm tracks), despite the fact that there are often significant differences in magnitude.

Figure 1 shows the zonally and annually averaged liquid water path over all surfaces for the standard CCM2 (case 414), the 5-yr numerical integration incorporating the revised liquid water formulation described in the previous section (case dlwp0), and a satellite-derived zonally averaged liquid water path (ocean only) using data obtained from Greenwald et al. (1995) for the 4-yr period 1988–91. Liquid water path was not an archived quantity in any of the CCM2 controls, so the values reported here were diagnostically computed from standard model output. Nonlinearities in this diagnostic procedure preclude an exact calculation of the

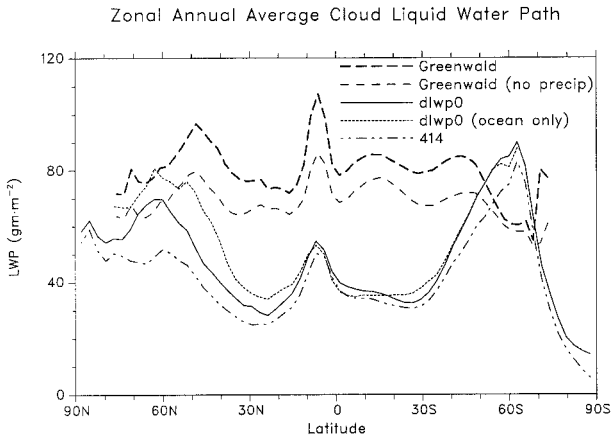

FIG. 1. Zonally and annually averaged cloud liquid water path (g m^{-2}) for CCM2, the diagnostic liquid cloud water model configuration (DLW), and the 1988–91 Greenwald et al. (1995) satellite retrievals for all-sky fields of view.

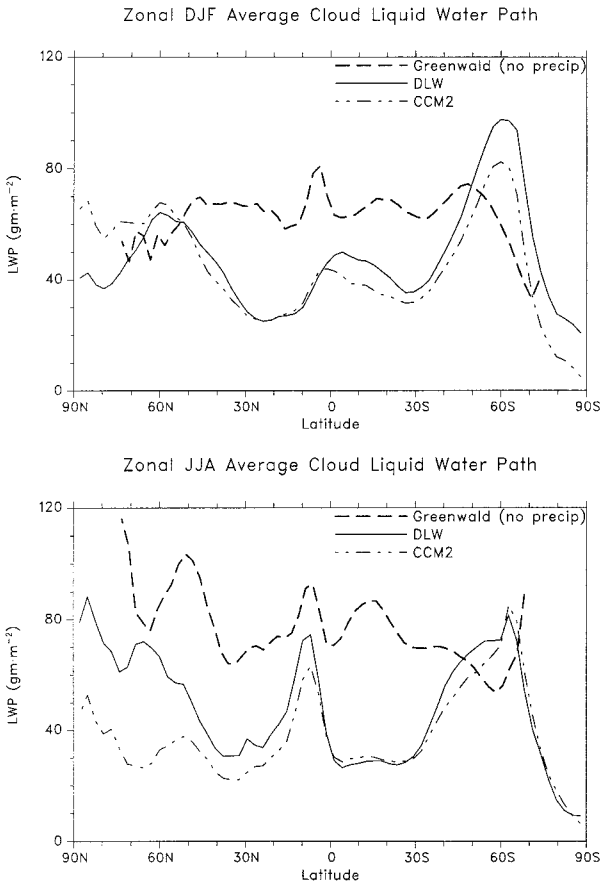

FIG. 2. Zonally averaged DJF and JJA cloud liquid water path (g m^{-2}) for CCM2, the DLW model configuration, and the 1988–91 Greenwald et al. (1995) satellite retrievals for nonprecipitating all-sky fields of view.

liquid water path, although tests of the procedure indicate that the zonal mean data should be accurate to less than 5%. Also note that the CCM2 does not distinguish between cloud water and cloud ice. Thus, the simulated cloud water data discussed in this section includes all condensate in the column.

The Greenwald data represent an *all-sky* field of view, where no thresholding has been applied to the data. This representation of the data is more consistent with the averaging process used for the simulated cloud liquid water path, since clear-sky conditions are included in the model-generated average. For this reason, the satellite-derived measures presented here are smaller in magnitude than the data presented in Greenwald et al. (1995), since the latter study was targeted at characterizing cloud properties and therefore excluded clear-sky fields of view as well as precipitating clouds. The two zonal mean satellite retrievals shown in Fig. 1 are for all sampled conditions and for conditions where the liquid water path data have been filtered to remove precipitating clouds (since the liquid water path retrievals are unreliable when precipitation is present). The two curves thus provide one measure of the expected uncertainty in the Greenwald et al. retrievals (in this case the effects of precipitating clouds), where the nonprecipitating conditions show approximately a 20% systematic reduction in the all-sky results. Since the satellite estimates are over ocean only, we have also included a zonal average curve for the DLW simulation using ocean-only data. The elimination of land and sea-ice points from the DLW zonal average does produce a noticeable change from the more complete zonal mean, where the Northern Hemisphere ocean-only liquid water distribution is clearly larger in magnitude.

The CCM2 and DLW results exhibit well-defined liquid water maxima in the extratropical storm tracks, along with a clear secondary maximum in the ITCZ. This is not the case for the satellite-derived cloud liquid water. There is a clear maximum in the ITCZ, but little meridional definition of extratropical features (e.g., the absence of well-defined subtropical minima). The Southern Hemisphere extratropical maximum seen in the simulated data is essentially nonexistent in the satellite data. The amplitude of the satellite-derived cloud liquid water path is also systematically and significantly larger than what is produced in the AGCM simulations, particularly in the Tropics. The lack of an extratropical maximum in the satellite retrievals may be related to the absence of column integrated ice condensate. Thus, the satellite-derived data underestimate the total condensate in the column where this underestimate may be particularly large at the higher latitudes.

The seasonal behavior of the simulated cloud liquid water is shown in Fig. 2, which includes the DJF and JJA zonally averaged liquid water path for CCM2 and DLW, along with the Greenwald estimates (for nonprecipitating conditions). These curves clearly demonstrate that the liquid water response to the new formulation is most pronounced in the summer hemisphere at high latitudes, where the DLW experiment exhibits a noticeable seasonal swing in liquid water path poleward of

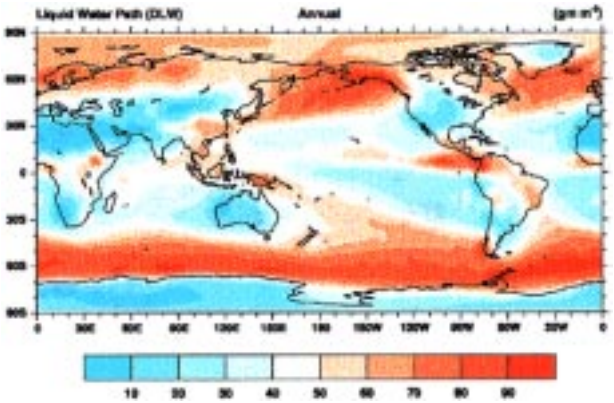

FIG. 3. Annually averaged cloud liquid water path distribution (g m^{-2}) for the DLW model configuration.

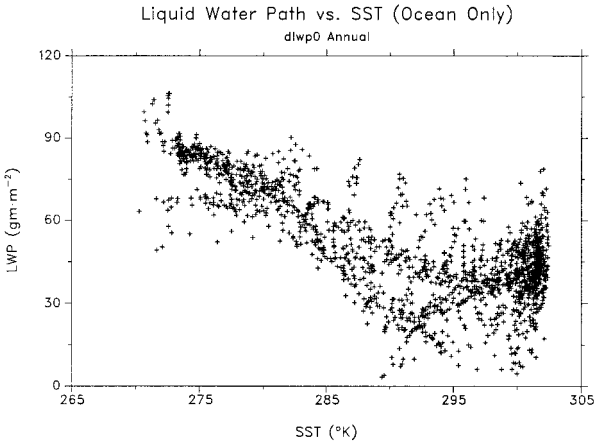

FIG. 4. Scatter diagram of annually averaged cloud liquid water path (g m^{-2}) vs sea surface temperature (K).

30°. The seasonal differences are largest in the Northern Hemisphere. During JJA, the zonally averaged liquid water path almost doubles poleward of 70°N. This strong seasonal oscillation in extratropical cloud liquid water is also seen in the satellite estimates, where similar relative changes occur (see also Fig. 6 in Greenwald et al. 1995). Interestingly, the CCM2 also exhibits a high-latitude seasonal oscillation in cloud liquid water, but with the opposite phase. The CCM2 behavior reflects the seasonal cycle in diagnosed cloud amount. The DLW cloud distribution exhibits a similar seasonal behavior, where properties of the cloud distribution in both model configurations are within observational uncertainty as determined by ISCCP (Rossow and Zhang 1995) and *Nimbus 7* (Hurrell and Campbell 1992). As in the case of the annual average meridional distribution shown in Fig. 1, the extratropical storm tracks and ITCZ are very well defined for the DLW experiment, where the seasonal distribution of the satellite-derived product continues to show little meridional definition, and no indication of a Southern Hemisphere storm track.

Figure 3 shows the annually averaged global distribution of the cloud liquid water path for the DLW simulation (which can be compared with Fig. 1 in Greenwald et al. 1995). Familiar climate features can be seen in this figure including the ITCZ, extratropical storm tracks, and South Pacific and South Atlantic convergence zones. Additionally, one can clearly see the stratocumulus subsidence regions in the eastern oceans, which are well defined by pronounced minima in the liquid water distribution as they are in the satellite-derived data. Maximum values of the cloud liquid water path locally exceed 100 g m^{-2}, occurring in both the ITCZ and extratropical storm track features (e.g., Gulf of Alaska). One notable characteristic of the simulated ITCZ is a relatively weak representation in both the central Pacific and central Atlantic Oceans. This apparent deficiency is partly the reflection of overly active convection regimes occurring in the eastern oceans, a well-known simulation bias in the CCM2. In many respects, there are a large number of similarities in the characteristics of the horizontal distribution of cloud liquid water when compared with the satellite-derived estimates. The most important differences appear to be the presence of larger and more clearly defined convectively suppressed subtropical regimes and an obvious Southern Hemisphere extratropical storm track in the simulated data. And, as suggested by the zonal means, the satellite-derived estimates are systematically larger in magnitude, where even the strongest features in the simulated liquid water path fall far short of comparable features in the satellite climatology.

Since the revised cloud liquid water parameterization ties the local liquid water scale height to precipitable water, and there are well-known positive correlations between precipitable water and SST, we examine whether SST exerts a strong influence on the diagnosed liquid water. Figure 4 shows a scatterplot of liquid water path versus SST, over ocean only, for the DLW experiment. The simulated liquid water path shows a clear negative correlation with SST (i.e., larger liquid water paths for lower SSTs), with some indication of a positive correlation at high temperatures, partly due to the increased scatter at high temperatures. The basic characteristics of the correlations in Fig. 4 reflect the meridional distribution of cloud liquid water path, which show a clear tendency for more cloud water at the higher latitudes (and lower SSTs) than in the Tropics. A similar scatterplot for the satellite retrievals reflects the relatively flat meridional distribution, with a slightly positive correlation between liquid water path and SST. In both cases, there is considerable (and similar) scatter in the liquid water path for any given SST, particularly for the higher range of SSTs.

Overall, the simulated liquid water distribution appears to be quite reasonable, although it exhibits significantly weaker amplitude when compared with the satellite derived data, especially in the Tropics. If cloud ice were to be included in the satellite estimates, this

TABLE 1. Global annual average properties for the CCM2 and DLW experiments, along with observational estimates.

	Observations	CCM2	DLW	DLWRE[f]
Outgoing longwave radiation (W m^{-2})				
all sky	234.8[a]	240.48	237.64	236.72
clear sky	264.0[a]	271.41	271.30	270.77
Absorbed solar radiation (W m^{-2})				
all sky	238.1[a]	244.95	240.93	237.96
clear sky	286.3[a]	294.96	294.96	294.91
Precipitable water (mm)	27.4[c]	25.22	25.34	24.76
Surface temperature (land)	282.9[e]	279.27	278.97	278.37
Latent heat flux (W m^{-2})	78.0[d]–90.1[e]	103.48	101.68	100.82
Sensible heat flux (W m^{-2})	15.0[d]	9.33	9.06	8.95
Net surface solar radiation (W m^{-2})	165.1[b]	180.60	176.68	174.13
Net surface longwave radiation (W m^{-2})	45.8[b]	62.65	61.93	62.42
Annual mean budgets (W m^{-2})				
TOA energy budget		4.47	3.29	1.24
Surface energy budget		5.14	4.01	1.94

[a] ERBE (Earth Radiation Budget Experiment).
[b] Rossow and Zhang (1995).
[c] ECMWF analyses.
[d] Kiehl and Trenberth (1997).
[e] Legates and Willmott (1990).
[f] DLW including effective radius modifications (see section 5).

discrepancy would be even larger. Since there is considerable uncertainty in the amplitude of cloud liquid water in the observational datasets, in the next section we examine the top-of-atmosphere radiation properties, which are much better-known quantities.

4. Mean-state response

We begin this discussion by presenting a selected list of global annual statistics in Table 1 for the CCM2 control simulation and for the DLW model configuration. These particular global averages are highly stable measures of model performance, where even relatively small differences indicate significant systematic changes in the properties of the simulation. The table shows important changes in all-sky TOA radiation metrics for the DLW experiment. Both the solar and longwave components have moved closer to observational estimates. Because the clear-sky fluxes (which exhibit moderate differences with observations) are basically unaffected by the changes to the cloud parameterization, the longwave cloud forcing (LWCF) and shortwave cloud forcing (SWCF) in the DLW simulation move a comparable distance farther away from their respective observational estimates. The more important surface response shows a nearly 4 W m^{-2} reduction in absorbed solar flux, which is partially offset by a 2 W m^{-2} reduction in the surface latent heat flux (and global precipitation rate). Surface temperature over land also shows a 0.3° cooling in the global annual mean, a response consistent with the reduced surface solar flux. Note that although the CCM2 global average surface temperature already exhibits a cold bias when compared to observations (dominated by systematically colder temperatures over Northern Africa and the Tibetan Plateau), the additional reduction for the DLW experiment is associated with desirable regional changes, as we will show. As suggested by the precipitable water entry, these changes in the global energy budget are not accompanied by significant differences in the globally or zonally averaged circulation characteristics. There are, however, some important regional circulation changes that we will illustrate in later sections. Generally speaking, seasonal zonal averages of temperature in the free atmosphere are within a few tenths of a degree of the control simulation, while seasonal zonal averages of specific humidity are well within several tenths of a g kg^{-1} of the CCM2 control. The most notable exceptions occur in the JJA lower-tropospheric simulation between 30° and 60°N, reflecting large changes to the simulated surface climate over land which will be illustrated later in this section.

a. TOA radiative characteristics

We will illustrate the changes in the TOA radiation budget by first examining the the seasonally and zonally averaged outgoing longwave radiation (OLR) and SWCF distribution, since they best show the respective changes in the longwave and shortwave components. The meridional distribution of seasonal TOA OLR and SWCF are shown in Figs. 5 and 6 for the Earth Radiation Budget Experiment (ERBE), the standard CCM2, and the DLW experiment. These figures clearly show that the principal TOA radiative response is confined to higher latitudes, particularly during the Northern Hemisphere summer months. The OLR exhibits an undesirable change in the Southern Hemisphere during DJF, but otherwise is improved, such as the better represen-

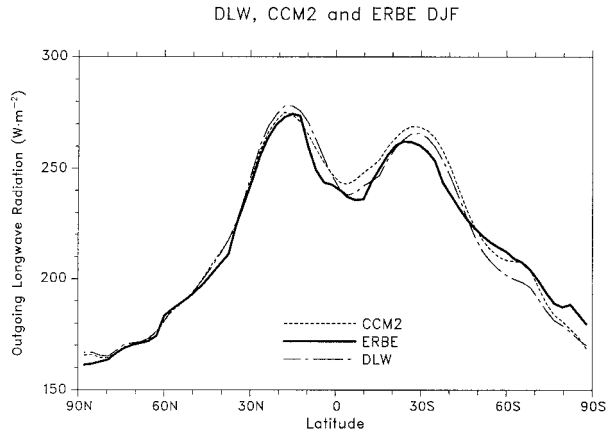

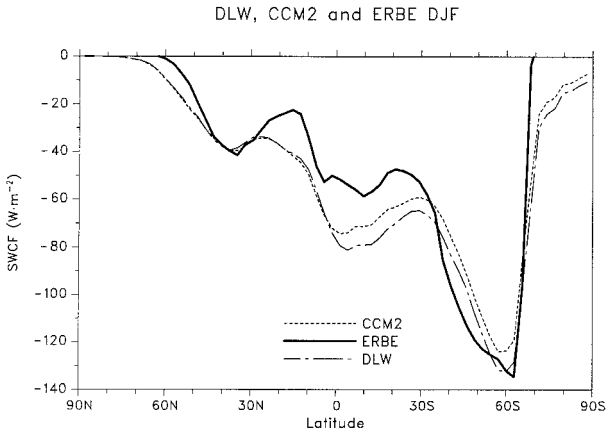

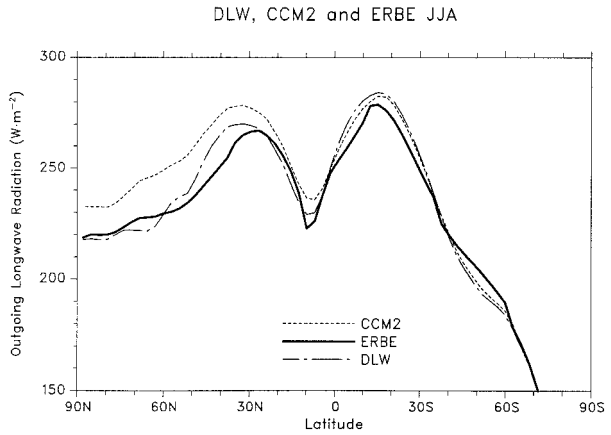

FIG. 5. Zonally averaged DJF and JJA OLR for CCM2, the DLW model configuration, and ERBE.

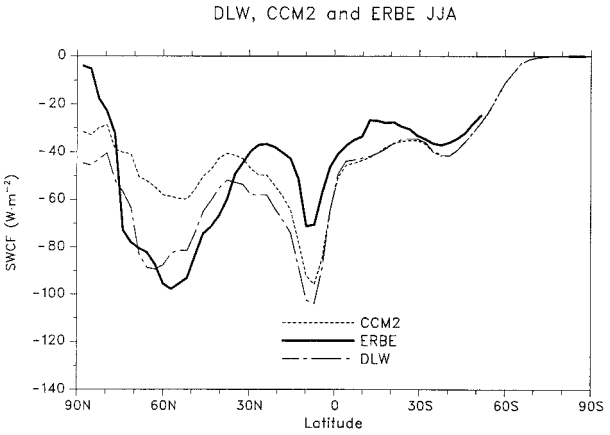

FIG. 6. Zonally averaged DJF and JJA SWCF for CCM2, the DLW model configuration, and ERBE.

tation of the ITCZ minimum. The most important response is seen in the JJA simulation where the OLR, which is severely overestimated poleward of 30°N in the CCM2, is reduced by as much as 24 W m^{-2} in the zonal mean. Examination of the LWCF distribution (not shown) indicates considerably better agreement with ERBE estimates over the Northern Hemisphere during JJA. The meridional asymmetry in subtropical LWCF during DJF is also much better represented in the DLW experiment.

As in the case of OLR, significant reductions in absorbed solar radiation (indicated by the SWCF curves) are seen in the respective summer hemispheres, where cloud forcing is dramatically enhanced in the summer hemisphere. Shortwave changes as large as 37 W m^{-2} occur during JJA near 70°N. Undesirable increases in summer hemisphere subtropical cloud forcing occur in both seasons, where existing biases are somewhat amplified. These biases are partially a deficiency in the diagnosis of cloud amount arising from the minimum 20% fractional cloud cover for nonprecipitating convective clouds. Changes to this part of the cloud fraction algorithm can help remedy the subtropical radiative bias without degrading other desirable features in the meridional distribution of cloud radiative forcing (e.g., see Kiehl et al. 1998).

Although the shortwave response is most pronounced (in absolute terms) over the Northern Hemisphere in JJA, the enhanced SWCF during DJF in the Southern Hemisphere storm track is also of importance. One of the CCM2 simulation deficiencies is that the annual mean implied meridional ocean heat transport does not agree well with observational estimates. It is in the wrong direction in the Southern Hemisphere, a fundamental problem for the development of a coupled atmosphere–ocean general circulation model. Gleckler et al. (1995) have shown that the meridional heat transport is critically sensitive to the radiative effects of clouds, in particular, the SWCF. The 12 W m^{-2} enhancement of the SWCF in the Southern Hemisphere storm track moves the cloud-forcing curve closer to the observational estimates, but surprisingly, it only marginally improves the characteristics of the implied ocean heat transport. This result suggests that deficiencies in the representation of cloud radiative forcing do not adequately account for the serious (but typical) errors in the CCM2 implied ocean heat transport. A more extensive investigation into the sources of anomalous merid-

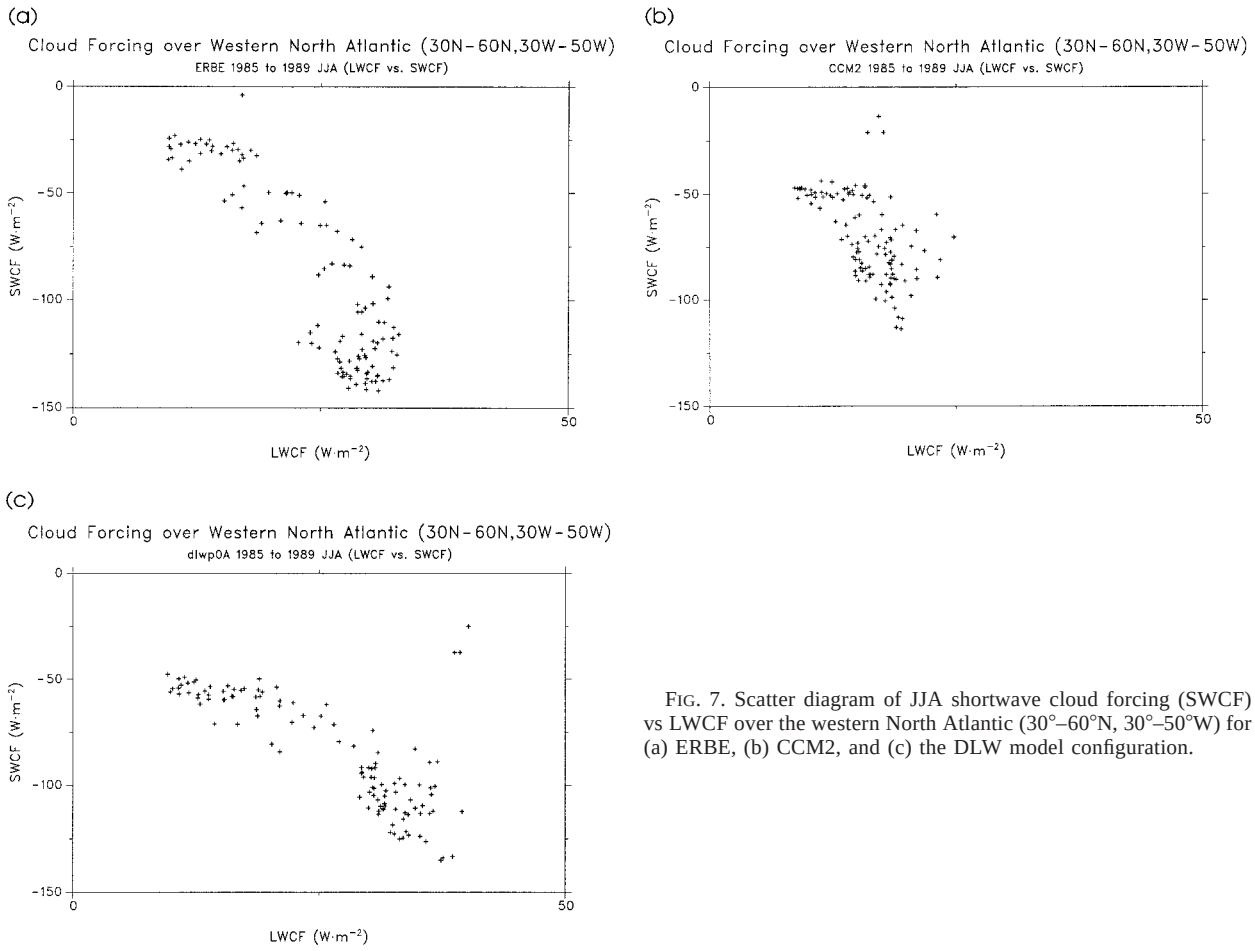

FIG. 7. Scatter diagram of JJA shortwave cloud forcing (SWCF) vs LWCF over the western North Atlantic (30°–60°N, 30°–50°W) for (a) ERBE, (b) CCM2, and (c) the DLW model configuration.

ional energy transport in the CCM can be found in Hack (1998).

Additional insight into the radiative changes associated with the DLW experiments can be seen from a regional examination of cloud forcing along the lines of Kiehl and Ramanathan (1990), who showed observational evidence for a near cancelation of cloud forcing in regions of deep tropical convection. In this regard, the CCM2 did a very credible job of capturing these radiative forcing characteristics in the Tropics, but failed to reproduce observed regional forcing distributions in the extratropics (e.g., see Kiehl et al. 1994). This particular property of the CCM2 tropical simulation is generally unchanged in the DLW experiment, although there are significant regional differences at higher latitudes. Figure 7 illustrates the relationship of LWCF to SWCF for a region in the western North Atlantic (30°–60°N, and 30°–50°W), during JJA, for ERBE, the CCM2 and the DLW experiment. These plots show that the CCM2 seriously underestimates both the LWCF and SWCF in this region. Since most of the TOA SWCF is felt at the surface, the SWCF differences seen in Fig. 7 suggest an anomalous surface solar flux excess of around 40 W m^{-2} over this very large region. The incorporation of the diagnostic liquid water parameterization significantly reduces these cloud-forcing errors at the higher latitudes, particularly with respect to the shortwave component of the energy budget.

Overall, the changes to the TOA radiative balance represent a marked improvement when compared to the standard CCM2. The improvements are especially noteworthy with respect to Northern Hemisphere JJA seasonal averages, and translate, as we will show, into large improvements in the simulated surface climate.

b. Surface climate

As mentioned earlier, the CCM2 JJA simulation exhibits a significant warm bias in surface temperature over most of the Northern Hemisphere, along with a systematic overprediction of precipitation. In an earlier study documenting the CCM2 climate, Hack et al. (1994) speculated (largely on the basis of deficiencies in the TOA radiative balance) that these biases were a consequence of inadequacies in the treatment of cloud optical properties. In the previous section, we showed that the introduction of the diagnostic procedure for cloud liquid water significantly improved the TOA ra-

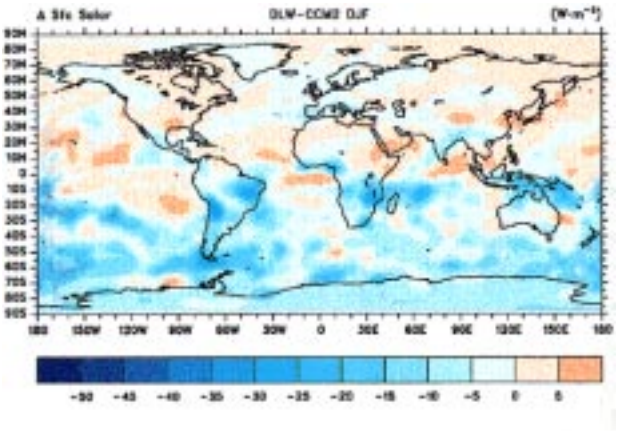

FIG. 8. Change in absorbed solar radiation at the surface (DLW–CCM2) for DJF and JJA.

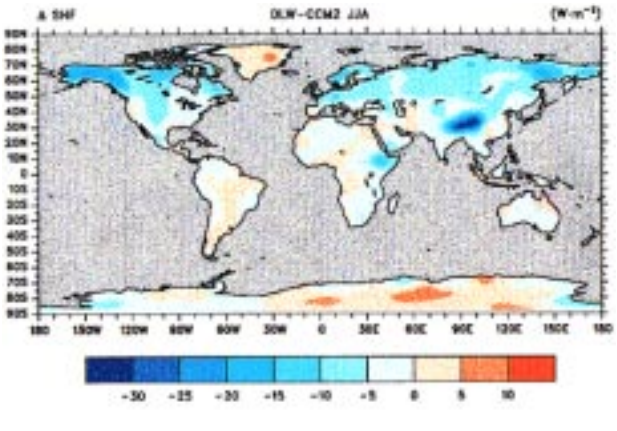

FIG. 9. Change in JJA sensible and latent heat fluxes (DLW–CCM2).

diative characteristics, which should be expected to benefit many of the CCM2 surface climate biases.

Changes in the surface climate arise largely in response to a sharp reduction in absorbed solar radiation at the surface (ASR_{sfc}). The change in ASR_{sfc} is illustrated in Fig. 8 for both DJF and JJA. The panels show a very large response in the respective summer hemispheres. The JJA changes are most pronounced, with large-scale systematic reductions in ASR_{sfc} primarily poleward of 30°N, where changes exceed 50 W m^{-2} locally. Note that the effects are largely independent of the underlying surface, although there is clearly a larger impact over land surfaces than there is over brighter snow- and ice-covered surfaces at the higher latitudes. The effective radius modifications we will incorporate later directly affect the radiative budget over land surfaces only.

The large reductions in ASR_{sfc} are reflected in comparable changes to the surface turbulent heat flux, as shown in Fig. 9 (where Δ's are defined to be DLW–CCM2). The panels show the difference in JJA seasonal means of sensible and latent heat flux, where each of these fields exhibit large spatially coherent decreases in the Northern Hemisphere. This widespread and sharp reduction in surface heat flux is in response to a cooling of the surface, which is also associated with decreased precipitation. The change in the global distribution of surface temperature and precipitation for the JJA seasonal means is shown in Fig. 10. We see a modest systematic reduction in each of these fields over the Northern Hemisphere continents, where T_s drops by more than 3 K locally at the higher latitudes, and total precipitation P decreases in both the midlatitudes and in convectively active tropical regions. Reductions in surface temperature represent as much as one-third of the respective local bias exhibited by the CCM2 JJA simulation. Many of the local precipitation reductions represent almost one-half of the previously existing bias (e.g., over the southeastern United States). The precipitation response appears to be directly attributable to cooler surface temperatures, which result in lower latent heat fluxes (because the CCM2 soil moisture is fixed) and reduced convective activity.

c. *Extratropical response*

Another of the more serious biases in the CCM2 DJF simulation is the anomalous extratropical stationary

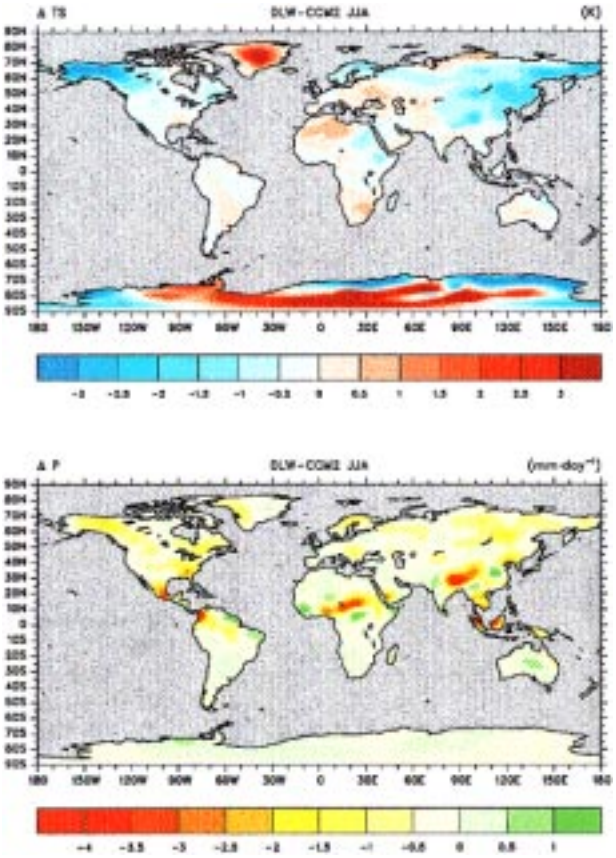

FIG. 10. Change in JJA surface temperature and precipitation (DLW–CCM2).

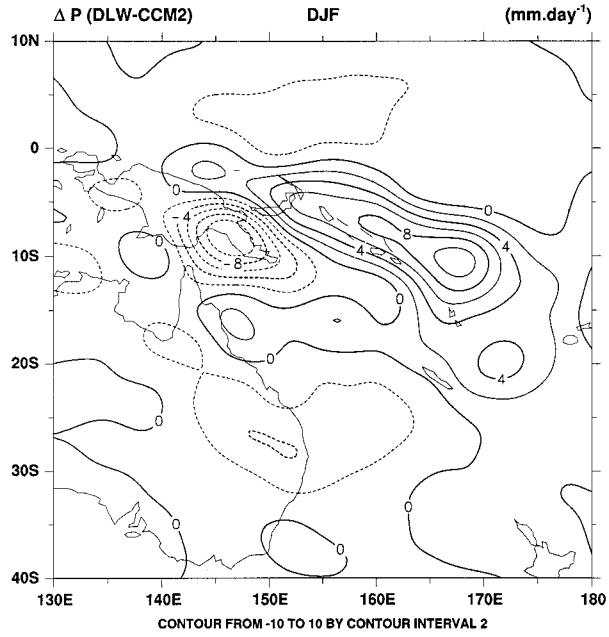

FIG. 11. Change in DJF precipitation in the western Pacific (DLW–CCM2).

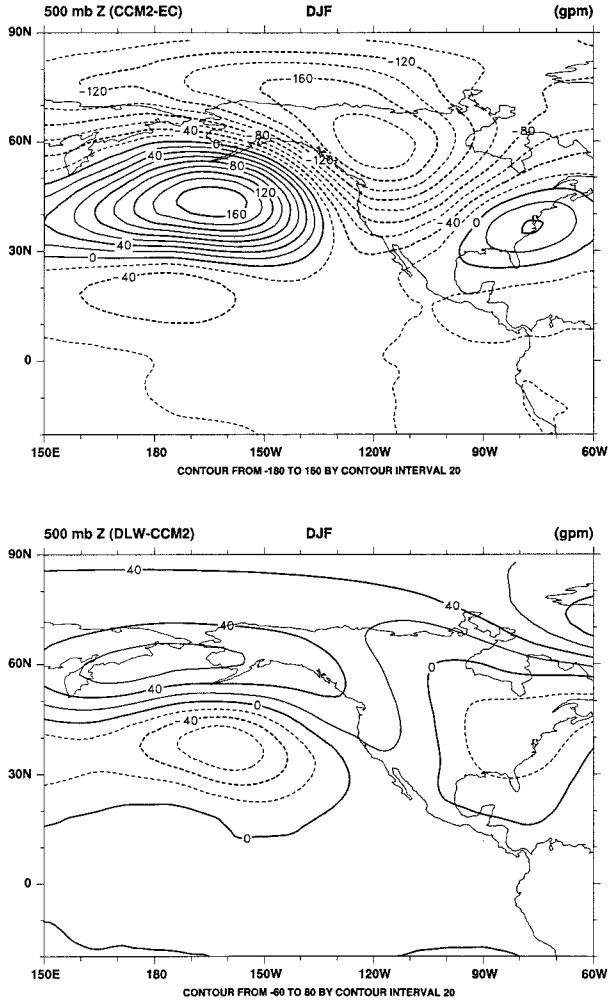

FIG. 12. (a) CCM2 DJF 500-mb height anomaly with respect to ECMWF analyses, and (b) the change in the DJF 500-mb height field associated with the introduction of the diagnostic liquid water parameterization (DLW–CCM2).

wave pattern over the Northern Hemisphere. An examination of the 500-mb geopotential height field shows that the CCM2 misplaces the observed ridge along the west coast of North America resulting in a positive height error over the North Pacific and a negative height error over western Canada. The error field resembles a reverse Pacific–North American (PNA) teleconnection pattern originating in the tropical western Pacific. Linear studies of barotropic energy dispersion (in the context of tropical–extratropical teleconnections) suggest that this type of stationary wave error may be a response to anomalous diabatic forcing in the tropical western Pacific (e.g., Hoskins and Karoly 1981; Branstator 1985; Sardeshmukh and Hoskins 1988).

An unexpected consequence of the changes to the liquid water formulation is a substantial reorganization of the DJF western Pacific precipitation pattern. The

large precipitation maximum in the CCM2 simulation is reduced, and the overall pattern exhibits a smoother horizontal distribution. A major feature of the resulting precipitation pattern is a significant reduction in precipitation over the eastern part of New Guinea and a comparably large increase in precipitation just east of the Solomon Islands, as shown in Fig. 11. There are also significant precipitation reductions in regions bounding this eastward shift (e.g., a large reduction in Australian monsoon precipitation). The associated change in diabatic heating is linked to a significant reduction in the midlatitude stationary wave error over the North Pacific and western North America as shown in Fig. 12 (DLW–CCM2). The 500-mb response exhibits a PNA structure with peak amplitudes exceeding 70 m, eliminating approximately one-third of the CCM2 stationary wave error over the North Pacific. We will revisit this response when we discuss the synergism between the diagnostic liquid water formalism introduced in this manuscript, and the cloud drop effective radius scheme proposed by Kiehl (1994).

5. Climate-change sensitivity

In the previous section, we illustrated important sensitivities in several aspects of the mean climate state to the introduction of a diagnostic cloud liquid water procedure. In this section we will explore the ''climate-change'' sensitivity of the CCM to this new physical parameterization. The first question we wish to address is how the diagnostic cloud liquid water scheme might affect the global average response to changes in forcing, such as changes in CO_2 concentration. We examine the climate sensitivity of the CCM using the experimental framework introduced by Cess and Potter (1988) and later used by Cess et al. (1990, 1996) in two intercomparison studies of atmospheric general circulation models (AGCMs). The purpose of the intercomparisons was to try to better understand cloud feedback processes that determine AGCM sensitivity to climate change scenarios. The procedure employs perturbations in sea surface temperature (SST) to serve as a surrogate climate change, where the cloud forcing response is examined to evaluate the model's climate sensitivity. This approach amounts to an inverse climate change experiment, where the climate change is imposed, and the model produces a corresponding change to its internal equilibrium. In particular, two numerical experiments are conducted for perpetual July conditions, one incorporating a constant $+2$ K SST perturbation and the other incorporating a -2 K SST perturbation. Sea ice and snow cover are fixed in each experiment (to eliminate surface albedo feedbacks) as is soil moisture (to prevent drying of the continents). The global average response to the imposed change in the surface climate is then evaluated in terms of a climate sensitivity parameter, λ,

$$\lambda = (\Delta F/\Delta T_s - \Delta Q/\Delta T_s)^{-1}, \tag{17}$$

TABLE 2. Climate sensitivity measures for CCM1, CCM2, and the diagnostic liquid water experiment.

	CCM1	CCM2	DLW
Climate sensitivity parameter (λ)	0.70	0.37	0.39
Cloud feedback parameter ($\Delta CRF/G$)	+0.63	−0.15	−0.11
longwave component	—	−0.54	−0.22
shortwave component	—	+0.39	+0.11

where F and Q respectively represent the global mean emitted infrared and net downward solar fluxes at the TOA. To help understand the cloud processes that contribute to the observed sensitivity, Cess et al. (1990) introduce a definition of cloud feedback, which employs the concept of cloud radiative forcing

$$\lambda/\lambda_c = 1 + \Delta CRF/G, \tag{18}$$

where G is a measure of direct radiative forcing at the TOA

$$G = \Delta F - \Delta Q, \tag{19}$$

CRF is the net TOA cloud radiative forcing, and λ_c is the clear-sky climate sensitivity parameter (i.e., λ for a fictitious clear-sky earth, principally a measure of water vapor and lapse rate effects). Thus, $\Delta CRF/G > 0$ denotes a positive cloud feedback, since it would imply an amplification of the direct radiative forcing (i.e., $\lambda/\lambda_c > 1$), $\Delta CRF/G = 0$ would correspond to zero cloud feedback, and $\Delta CRF/G < 0$ would indicate a negative cloud feedback.

The Cess et al. (1990) intercomparison demonstrated almost a threefold variation in the climate sensitivity parameter for the 19 participating AGCM's, where this variation was largely attributable to cloud feedback processes. The CCM1 exhibited a climate sensitivity parameter on the high side of the distribution with a modest positive cloud feedback (see Table 2). These sensitivity characteristics are substantially different for the CCM2, which exhibits a much smaller climate sensitivity parameter and a modest negative cloud feedback (e.g., see Cess et al. 1996). A more detailed examination of the cloud feedback parameter, $\Delta CRF/G$, shows that this negative cloud feedback is the result of a slightly stronger negative feedback in the longwave component when compared to the positive feedback exhibited by the shortwave cloud component, as shown in Table 2.

Evaluation of these climate sensitivity metrics for the DLW configuration of CCM2 reveals mixed results when compared to the control model. The climate sensitivity parameter is essentially unchanged (i.e., within natural variability), where the cloud feedback parameter suggests a very slightly more neutral behavior. Examination of the longwave and shortwave components of ($\Delta CRF/G$) shows that the magnitudes have been reduced substantially, by more than a factor of 2 in the longwave component and almost a factor of 4 in the shortwave component. So, although the overall cloud feedback remains quite similar to the CCM2, the DLW

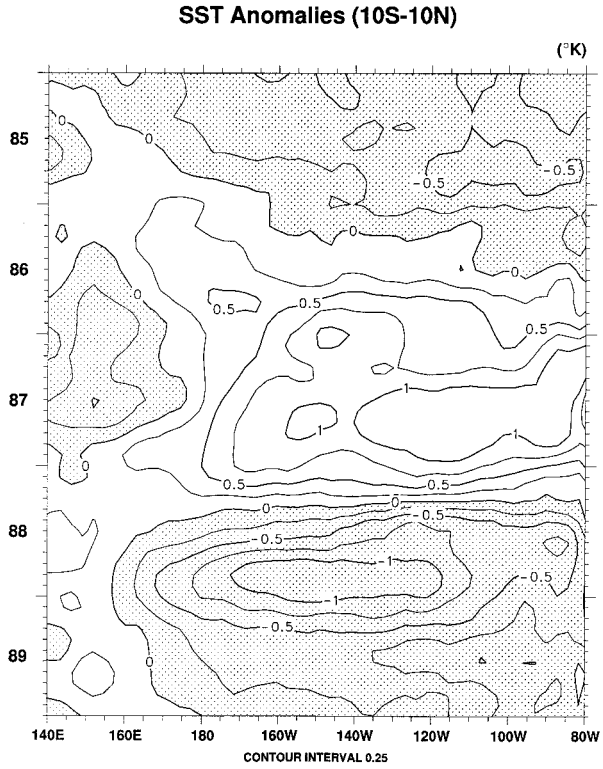

FIG. 13. Equatorial (10°N–10°S) SST anomalies for the 5-yr period 1985–89.

configuration achieves this with a longwave–shortwave balance that is among the smaller of the feedbacks exhibited in the most recent cloud feedback intercomparison (see Cess et al. 1996). These results suggest that the basic climate sensitivity exhibited by the CCM2 and DLW simulations is linked to the specified profile for in-cloud liquid water concentration. Changes to the formulation of cloud optical properties (including cloud drop effective radius) affect the cloud feedback component details, but have little effect on the overall cloud feedback or climate sensitivity of the model.

Another way to evaluate the model sensitivity to climate change is to examine its response to El Niño–Southern Oscillation (ENSO). Equatorial SST anomalies associated with ENSO provide a useful framework for evaluating well-observed local and extratropical TOA radiative (and dynamical) responses in an AGCM climate simulation. Here, we examine the sensitivity of 5-yr CCM simulations forced with observed SSTs for 1985–89. This period includes a moderate warm SST event in 1987 followed by a strong cold event in 1988 (as shown in Fig. 13). ERBE provides a unique observational dataset on cloud radiative forcing for this period, which can be used to evaluate the CCM's response to ENSO forcing. We first examine the model response in terms of equatorial TOA radiative anomalies. Figure 14 includes Hovmöller diagrams showing the TOA OLR anomalies as measured by ERBE over the equatorial region (averaged between 10°N and 10°S) for the period February 1985–May 1989, as well as for the CCM2 and DLW model-generated solutions. The ERBE measurements show a strong TOA response in OLR corresponding to the anomalies in SST, principally over the west central Pacific. During early 1987, the warm phase OLR anomaly clearly extends across the entire Pacific basin. Although the CCM2 control does a credible job of capturing the west central Pacific response, the eastern Pacific OLR anomaly is only weakly represented (e.g., see also Chen et al. 1995). The DLW experiment significantly improves upon the CCM2 results. The west-central Pacific anomalies are better represented in terms of their magnitude and structure, and the eastward extension of the OLR minimum in early 1987 is also very accurately captured.

The simulated ENSO response can also be illustrated by examining longer-term average differences between a warm and cold event. Figure 15 shows the seasonal difference in OLR between DJF 1987 and DJF 1989 (i.e., warm minus cold event) for ERBE, the CCM2, and the DLW experiment. The ERBE measurements show a sizable TOA reduction in OLR over the central Pacific, flanked by significant increases in OLR in the SPCZ and over the Hawaiian Islands. Although the CCM2 captures the basic structure of this response, it is too weak and displaced too far to the west. The DLW experiment does a much better job in reproducing the observed TOA response. The minimum in OLR is comparable in magnitude and location, as are the maxima in OLR on the northern and southern flank. These results represent a significant improvement in the simulated TOA radiative properties of the cloud field with the incorporation of the diagnostic liquid water formalism.

As a final measure of the simulated climate sensitivity, we consider a more complete description of the TOA radiation response to ENSO in the form of the cloud-radiative forcing. Figure 16 shows the relationship of the change in longwave cloud forcing (δ LWCF = $\mathrm{LWCF}_{\mathrm{MAM1987}}$–$\mathrm{LWCF}_{\mathrm{MAM1985}}$) to the change in shortwave cloud forcing (δ SWCF = $\mathrm{SWCF}_{\mathrm{MAM1987}}$–$\mathrm{SWCF}_{\mathrm{MAM1985}}$) for ERBE, the CCM2, and the DLW experiment over the tropical Pacific. The ERBE data show a very strong correlation in these quantities, suggesting that changes in longwave cloud forcing tend to be largely offset by comparable changes in shortwave cloud forcing (e.g., Ramanathan and Collins 1991). The CCM2 exhibits a similar relationship in these cloud measures, although the range in the two cloud-forcing components is noticeably smaller and more poorly correlated. The DLW experiment shows a clear improvement in the relationship of the cloud-forcing components, where the observed range is better represented, and the correlation between longwave and shortwave changes is slightly better.

6. Effective radius sensitivity

In this section, we consider the combined effects of the cloud drop effective radius parameterization intro-

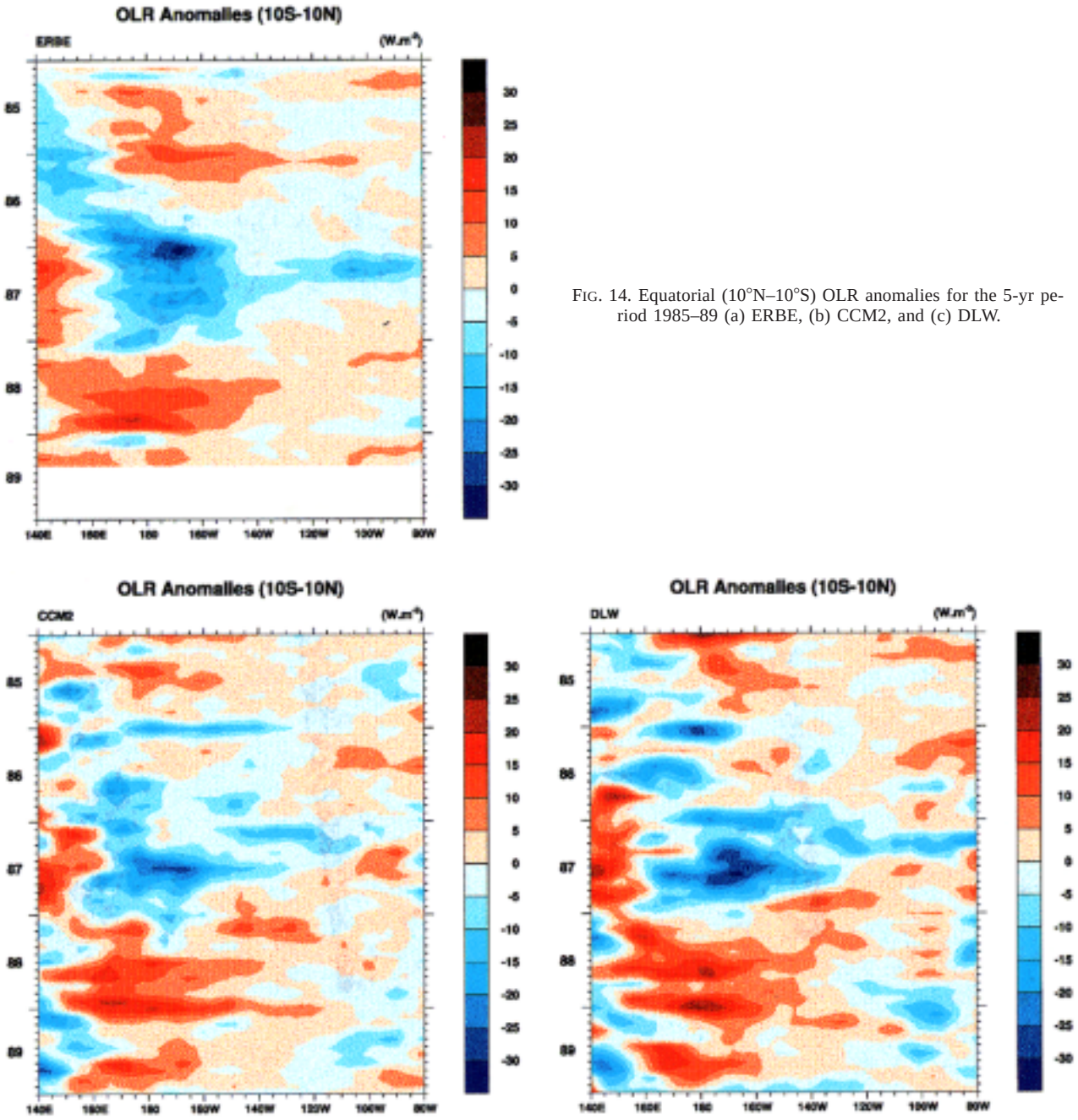

FIG. 14. Equatorial (10°N–10°S) OLR anomalies for the 5-yr period 1985–89 (a) ERBE, (b) CCM2, and (c) DLW.

duced by Kiehl (1994) and the diagnostic liquid water formulation introduced in section 2. The cloud drop effective radius scheme makes a distinction between continental and ocean liquid water clouds. Since only continental clouds are assigned a different effective radius (5 μm as opposed to 10 μm for maritime clouds), the principal climate response occurs over land areas where the direct radiative effects are felt only in the shortwave part of the radiation budget. Kiehl's examination of the simulated climate sensitivity demonstrated a large number of the same sensitivities to the mean state as shown in earlier sections. The question we address here is whether these improvements ''linearly'' complement each other, further improving the quality of the simulation, or whether their combination results in undesirable changes to the simulated climate.

A selected set of globally and annually averaged metrics are shown in Table 1 for CCM2 and the DLW and

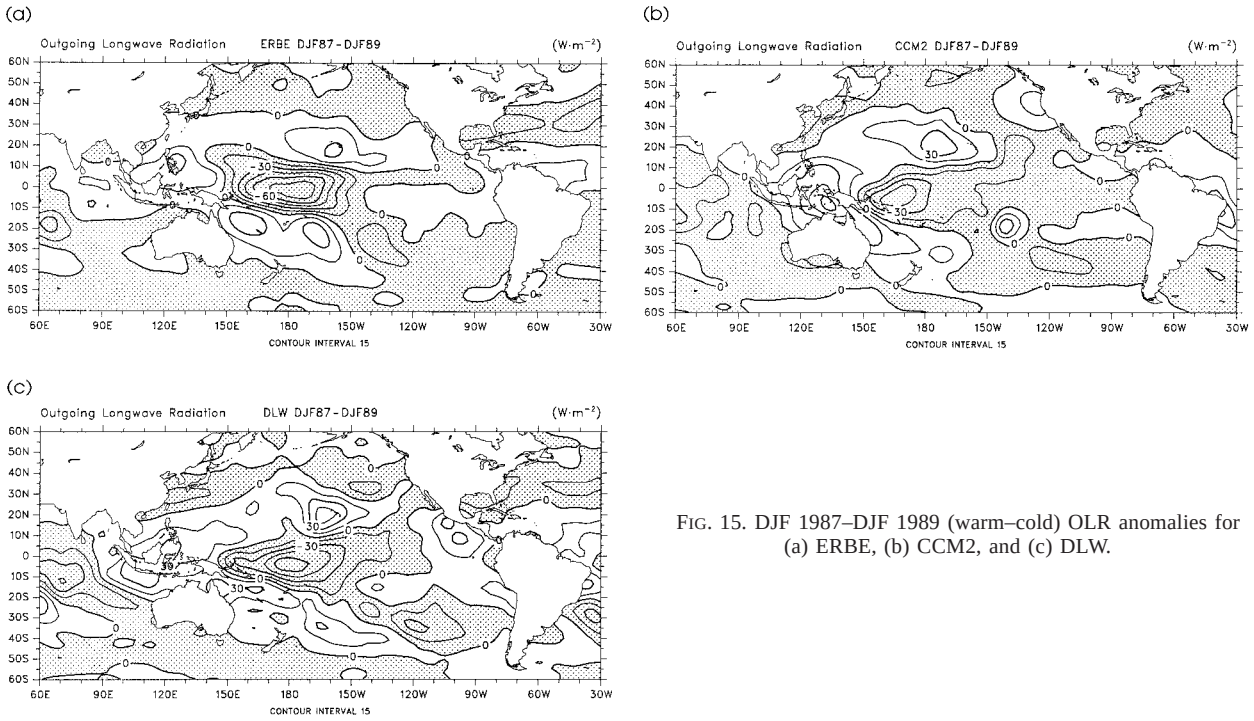

FIG. 15. DJF 1987–DJF 1989 (warm–cold) OLR anomalies for (a) ERBE, (b) CCM2, and (c) DLW.

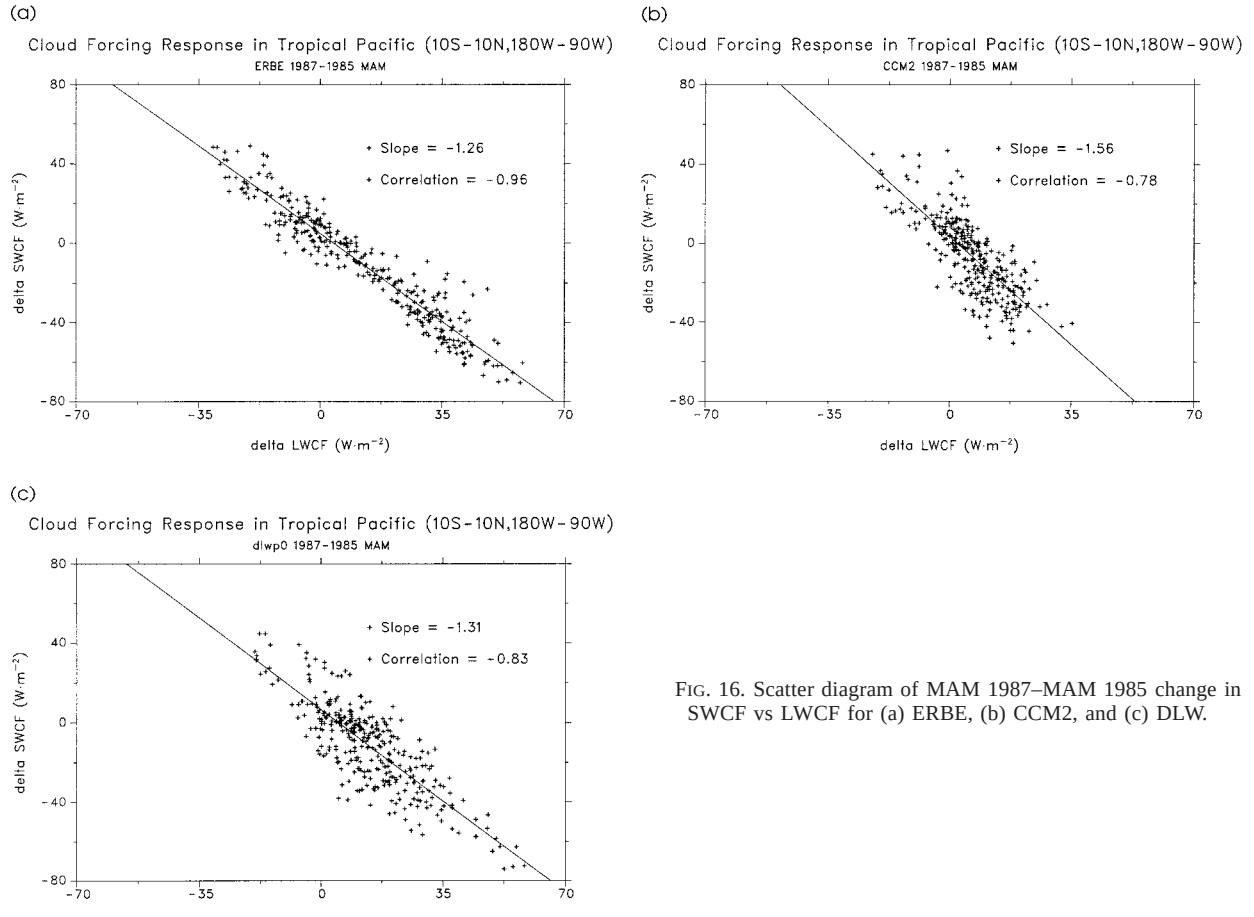

FIG. 16. Scatter diagram of MAM 1987–MAM 1985 change in SWCF vs LWCF for (a) ERBE, (b) CCM2, and (c) DLW.

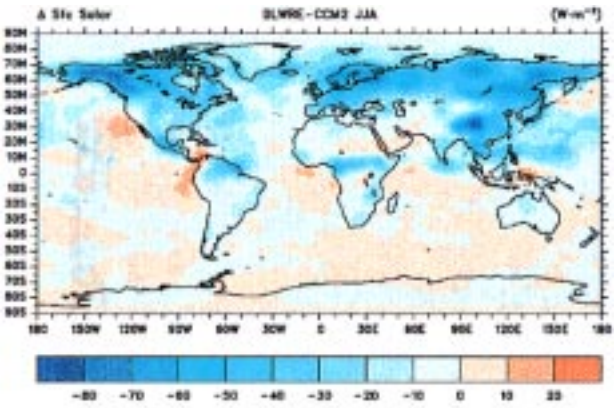

FIG. 17. Change in JJA surface absorbed solar radiation and surface latent heat flux (DL-WRE–CCM2).

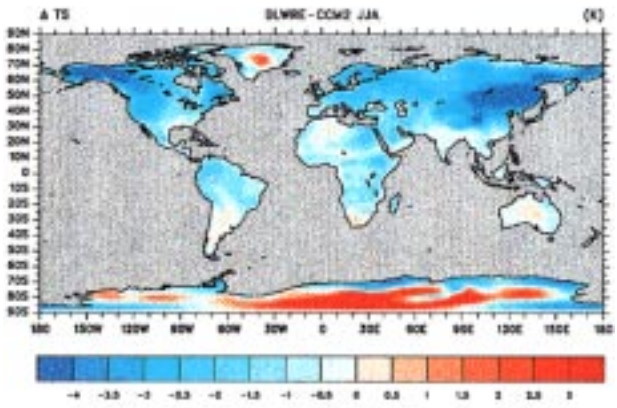

FIG. 18. Change in JJA surface temperature and precipitation (DLWRE–CCM2).

DLWRE (which includes the effective radius modifications) simulations. The major impact of the effective radius parameterization is on the shortwave radiation budget at both the TOA and surface, as would be expected. A small but noticeable reduction in precipitable water, primarily from decreases in precipitable water over the Northern Hemisphere land areas during the summer months, results in a slightly smaller reduction in absorbed solar radiation at the surface. The decreased surface solar flux is reflected in additional reductions to the turbulent surface heat flux. Another significant change is the continued decrease in globally averaged land surface temperature, where the DLWRE results are almost 1 K lower than in the CCM2 control.

Figure 17 shows seasonal JJA change in ASR_{sfc} and latent heat flux between the DLWRE simulation and CCM2 control (DLWRE–CCM2). We see that the changes in the annually averaged global means for these quantities translate into substantial seasonal departures from the control. Absorbed solar flux at the surface is locally reduced by more than 80 W m^{-2}, where the zonal mean is reduced by as much as 55 W m^{-2}. As we saw in section 4, this change is reflected in large systematic reductions in latent and sensible heat fluxes. Local decreases in the latent heat flux alone exceed 50 W m^{-2}. Regions of deep tropical convection also show similar signatures in ASR_{sfc} and surface heat flux. Figure 18 illustrates the global distribution of surface temperature and precipitation differences, showing quite large local differences in these fields. The combined effects of the cloud optical property modifications result in highly desirable improvements to the simulated surface climate. The continents exhibit large systematic reductions in surface temperature and precipitation. Many of the CCM2 precipitation biases, such as excessive precipitation over elevated terrain (e.g., over the Tibetan Plateau and Rocky Mountains), are largely eliminated with these modifications. Finally, the extratropical response to changes in the western Pacific precipitation distribution is enhanced with the addition of the effective radius parameterization, such that the CCM2 stationary wave error pattern is further reduced. This bias is almost eliminated over the North Pacific, and nearly cut in half over the western part of North America, as shown in Fig. 19.

7. Concluding remarks

We have presented a very simple diagnostic parameterization for in-cloud liquid water, which involves

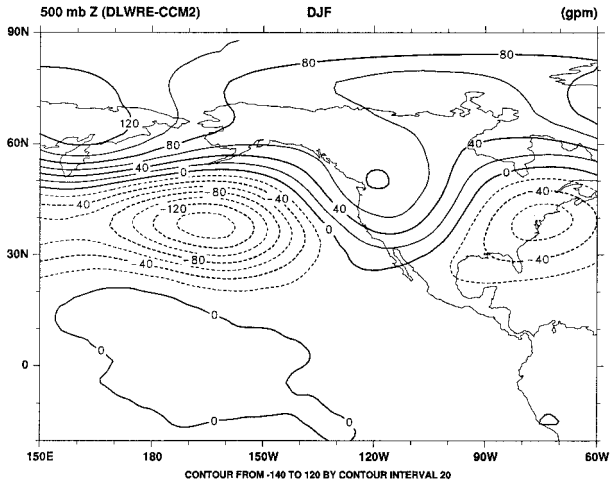

FIG. 19. Change in the DJF 500-mb height field associated with cloud liquid water and effective radius formulation (DLWRE–CCM2).

only a minor modification to the NCAR CCM2 cloud parameterization. The cloud liquid water diagnosed by this scheme captures the major climatological cloud features of the general circulation. The zonally averaged liquid water path exhibits extratropical maxima associated with the storm tracks and a secondary maximum associated with the ITCZ. A strong seasonal cycle is also seen at high latitudes, particularly over the Northern Hemisphere where the JJA zonally averaged liquid water path can be more than twice as large as the comparable DJF distribution. Despite the fact that the formalism links in-cloud liquid water to precipitable water, which is generally positively correlated with SST, the diagnosed liquid water path exhibits a weak negative correlation with SST.

Although the amplitude of the diagnosed liquid water path distribution is weaker than satellite-derived climatologies, the top-of-atmosphere radiation budget is in very good agreement with observational estimates. Globally averaged outgoing longwave and absorbed solar radiation are generally improved with the introduction of the liquid water scheme. A number of other systematic simulation biases, such as anomalously warm JJA surface temperatures and hydrologic cycle strength, are also reduced as indicated by changes in global annual averages. A more detailed analysis of these globally averaged changes shows that the most significant improvements to the global radiation budget occur at high latitudes, where errors in excess of 20 W m^{-2} in both the longwave and shortwave components of the budget are mostly eliminated. Although biases in cloud radiative forcing remain in the simulated results, a large component of which is associated with errors in the clear-sky fluxes (e.g., see Kiehl et al. 1997), the overall character of the longwave and shortwave cloud forcing is improved as shown by zonal and regional analyses.

The large differences between simulated and satellite-derived liquid water paths, where the simulated TOA radiation budget is in very close agreement with observations, is an intriguing result. It is particularly interesting because the largest differences occur in the Tropics, where the simulated shortwave cloud forcing is already a bit too large. Additional cloud water (as suggested by the satellite-derived climatology) and cloud ice (not included in the satellite estimates) would only serve to make the shortwave TOA bias worse. A preliminary single-column model sensitivity analysis suggests that the additional bias implied by the differences in tropical cloud water could not be remedied with reasonable changes in cloud drop radius. And, as mentioned earlier, the simulated cloud fraction in this region is already in good agreement with observational estimates. Therefore, the discrepancy in the microwave retrievals and parameterized shortwave radiative transfer represents an interesting scientific opportunity to better understand the relationship between large-scale cloud water (e.g., subgrid-scale variability issues, cloud particle size distributions, enhanced shortwave cloud absorption) and the treatment of parameterized radiative transfer in AGCMs.

Desirable changes in the surface climate, principally over the Northern Hemisphere, accompany the improvements in the top-of-atmosphere radiation budget. The large reductions in TOA absorbed solar radiation are also manifested at the surface. With these reductions in surface energy, the surface temperature over the high northern latitudes is significantly and systematically reduced during Northern Hemisphere summer. These surface temperature changes help to alleviate one of the more severe CCM2 simulation biases. Since soil moisture in the CCM2 is fixed, the reductions in surface temperature result in large decreases in latent heat flux and precipitation over land. Local changes in precipitation represent as much as one-half of the bias present in the CCM2, and the globally averaged changes contribute to a less vigorous hydrologic cycle (e.g., see Hack et al. 1998). Even tropical maxima are noticeably reduced where, for example, the CCM2 western Pacific DJF maximum in precipitation (near New Guinea) is reduced by approximately 15%.

An unexpected consequence of the cloud optical property change is an eastward migration of the January western Pacific precipitation maxima and an associated reduction in the midlatitude stationary wave error over the North Pacific and western North America. This extratropical response is similar to the cloud drop effective radius sensitivity seen in Kiehl (1994) and accounts for as much as one-third of the large CCM2 simulation bias.

An examination of the revised model's climate change sensitivity yields two major conclusions. First, the global climate sensitivity is basically unchanged, exhibiting a comparable climate sensitivity parameter. The way in which this sensitivity is achieved is different, however, where offsetting longwave and shortwave cloud feedback measures are much weaker in the revised model.

Second, an examination of the simulated ENSO response shows a marked improvement in top-of-atmosphere characteristics. Spatial shifts in cloud radiative forcing suggest improvements in the dynamical response as well. The observed cloud forcing response to ENSO is also well captured in the revised model, indicating a modest improvement when compared to the standard CCM2.

The combination of the effective radius scheme introduced by Kiehl (1994) with the diagnostic liquid water formulation results in even greater improvements to the simulated climate. Top-of-atmosphere radiation measures are further improved, particularly in the shortwave budget over the Northern Hemisphere, which is reflected in additional improvements in the simulated surface climate. Overall, the Northern Hemisphere surface temperature bias is reduced by almost two-thirds. Precipitation biases over warm land areas are also significantly reduced when compared with CCM2. Even the extratropical midtropospheric stationary wave pattern is further improved so that major features of the CCM2 height anomaly are substantially reduced or eliminated. Climate sensitivity measures, including the simulated ENSO response, are unchanged. This combination of modifications to the evaluation of cloud optical properties produces reductions in a wide range of simulation biases with little or no degradation of other climate measures. Because of the clear simulation advantages, the diagnostic cloud liquid water procedure in combination with the effective radius scheme proposed by Kiehl (1994) forms the basis for the diagnosis of cloud optical properties in the CCM3 (see Kiehl et al. 1996). Although such a simple diagnostic approach cannot capture many of the cloud phenomena represented in more complex prognostic cloud schemes, it does demonstrate superior simulation results when compared to the CCM2 with a negligible increase in computational cost.

Acknowledgments. I would like to acknowledge several exchanges regarding this work with Minghua Zhang, Dave Randall, and Tony Del Genio. I am particularly grateful to Jeff Kiehl for his comments on an early version of this manuscript and for his valuable perspective throughout the course of the work, and to David L. Williamson (DLW) for an especially insightful 1994 conversation somewhere over Iowa. Thanks also to Tom Greenwald for providing the satellite retrievals of cloud liquid water path used in this study. Finally, I wish to acknowledge Dave Randall for his support of a collaborative leave at Colorado State University, during which this manuscript was completed. This work was partially supported by the Computer Hardware Advanced Mathematics Model Physics (CHAMMP) Program, which is administered by the Office of Energy Research under the Office of Health and Environmental Research in the Department of Energy Environmental Sciences Division, and by the DOE ARM program.

REFERENCES

Betts, A. K., and Harshvardhan, 1987: Thermodynamic constraint on the cloud liquid water feedback in climate models. *J. Geophys. Res.,* **92,** 8483–8485.

Branstator, G., 1985: Analysis of general circulation model sea-surface temperature anomaly simulations using a linear model. Part I: Forced solutions. *J. Atmos. Sci.,* **42,** 2225–2241.

Briegleb, B. P., 1992: Delta-Eddington approximation for solar radiation in the NCAR Community Climate Model. *J. Geophys. Res.,* **97,** 7603–7612.

Cess, R. D., and G. L. Potter, 1988: A methodology for understanding and intercomparing atmospheric climate feedback processes in general circulation models. *J. Geophys. Res.,* **93,** 8305–8314.

——, and Coauthors, 1990: Intercomparison and interpretation of climate feedback processes in nineteen atmospheric general circulation models. *J. Geophys. Res.,* **95,** 16 601–16 615.

——, and Coauthors, 1996: Cloud feedback in atmospheric general circulation models: An update. *J. Geophys. Res.,* **101,** 12 791–12 794.

Chen, M., R. D. Cess, and M.-H. Zhang, 1995: Effects of longwave cloud radiative forcing anomalies on the atmospheric response to equatorial sea surface temperature anomalies. *J. Geophys. Res.,* **100,** 13 791–13 810.

Del Genio, A. D., M. S. Yao, W. Kovari, and K.-W. Lo, 1996: A prognostic cloud water parameterization for global models. *J. Climate,* **9,** 270–304.

Fowler, L. D., D. A. Randall, and S. A. Rutledge, 1996: Liquid and ice cloud microphysics in the CSU general circulation model. Part I: Model description and simulated microphysical processes. *J. Climate,* **9,** 489–529.

Gleckler, P. J., and Coauthors, 1995: Cloud radiative effects on implied oceanic energy transports as simulated by atmospheric general circulation models. *Geophys. Res. Lett.,* **22,** 791–794.

Greenwald, T. J., G. L. Stephens, S. A. Christopher, and T. H. Vonder Haar, 1995: Observations of the global characteristics and regional radiative effects of marine cloud liquid water. *J. Climate,* **8,** 2928–2946.

Hack, J. J., 1998: Analysis of the improvement in implied meridional ocean energy transport as simulated by NCAR CCM3. *J. Climate,* **11,** 1237–1244.

——, B. A. Boville, B. P. Briegleb, J. T. Kiehl, P. J. Rasch, and D. L. Williamson, 1993: Description of the NCAR Community Climate Model (CCM2). NCAR Tech. Note NCAR/TN-382+STR, National Center for Atmospheric Research, Boulder, CO, 108 pp. [NTIS PB93-221802/AS.]

——, ——, J. T. Kiehl, P. J. Rasch, and D. L. Williamson, 1994: Climate statistics from the NCAR Community Climate Model (CCM2). *J. Geophys. Res.,* **99,** 20 785–20 813.

——, J. T. Kiehl, and J. W. Hurrell, 1998: The hydrologic and thermodynamic characteristics of the NCAR CCM3. *J. Climate,* **11,** 1179–1206.

Hoskins, B., and D. J. Karoly, 1981: The steady linear response of a spherical atmosphere to thermal and orographic forcing. *J. Atmos. Sci.,* **38,** 1179–1196.

Hurrell, J. W., and G. G. Campbell, 1992: Monthly mean global satellite data sets available in CCM history tape format. NCAR Tech. Note NCAR/TN-371+STR, National Center for Atmospheric Research, Boulder, CO, 94 pp.

——, J. J. Hack, and D. P. Baumhefner, 1993: Comparison of NCAR Community Model Climates. NCAR Tech. Note NCAR/TN-395+STR, Boulder, CO, 335 pp.

Kiehl, J. T., 1994: Sensitivity of a GCM climate simulation to differences in continental versus maritime cloud drop size. *J. Geophys. Res.,* **99,** 23 107–23 115.

——, and V. Ramanathan, 1990: Comparison of cloud forcing derived from the Earth Radiation Budget Experiment with that simulated by the NCAR Community Climate Model. *J. Geophys. Res.,* **95,** 11 679–11 698.

——, and B. P. Briegleb, 1991: A new parameterization of the ab-

sorptance due to the 15-μm band system of carbon dioxide. *J. Geophys. Res.,* **96,** 9013–9019.

——, and K. E. Trenberth, 1997: Earth's annual global mean energy budget. *Bull. Amer. Meteor. Soc.,* **78,** 197–208.

——, R. J. Wolski, B. P. Briegleb, and V. Ramanathan, 1987: Documentation of radiation and cloud routines in the NCAR Community Climate Model (CCM1). NCAR Tech. Note NCAR/TN-288+IA, Boulder, CO.

——, J. J. Hack, and B. P. Briegleb, 1994: The simulated earth radiation budget of the NCAR CCM2 and comparisons with the Earth Radiation Budget Experiment (ERBE). *J. Geophys. Res.,* **99,** 20 815–20 827.

——, J. J. Hack, G. B. Bonan, B. A. Boville, B. P. Briegleb, D. L. Williamson, and P. J. Rasch, 1996: Description of the NCAR Community Climate Model (CCM3). NCAR Tech. Note NCAR/TN420+STR, National Center for Atmospheric Research, Boulder, CO, 152 pp.

——, ——, ——, ——, D. L. Williamson, and P. J. Rasch, 1998: The National Center for Atmospheric Research Community Climate Model: CCM3. *J. Climate,* **11,** 1131–1150.

Legates, D. R., and C. J. Willmott, 1990: Mean seasonal and spatial variability in gage-corrected, global precipitation. *Int. J. Climatol.,* **10,** 111–127.

Lin, B., and W. B. Rossow, 1994: Observations of cloud liquid water path over oceans: Optical and microwave remote sensing methods. *J. Geophys. Res.,* **99,** 20 907–20 927.

Njoku, E. G., and L. Swanson, 1983: Global measurements of sea surface temperature, wind speed, and atmospheric water content from satellite microwave radiometry. *Mon. Wea. Rev.,* **111,** 1977–1987.

Prabhakara, C., I. Wang, A. T. C. Chang, and P. Gloersen, 1983: A statistical examination of Nimbus 7 SMMR data and remote sensing of sea surface temperature, liquid water content in the atmosphere, and surface wind speed. *J. Climate Appl. Meteor.,* **22,** 2023–2037.

Ramanathan, V., and W. Collins, 1991: Thermodynamic regulation of ocean warming by cirrus clouds deduced from observations of the 1987 El Niño. *Nature,* **351,** 27–32.

——, E. J. Pitcher, R. C. Malone, and M. L. Blackmon, 1983: The response of a spectral general circulation model to refinements in radiative processes. *J. Atmos. Sci.,* **40,** 605–630.

Rossow, W. B., and Y.-C. Zhang, 1995: Calculation of surface and top of atmosphere radiative fluxes from physical quantities based on ISCCP data sets 2. Validation and first results. *J. Geophys. Res.,* **100,** 1167–1197.

Sardeshmukh, P. D., and B. J. Hoskins, 1988: The generation of global rotational flow by steady idealized tropical divergence. *J. Atmos. Sci.,* **45,** 1228–1251.

Slingo, A., 1989: A GCM parameterization for the shortwave radiative properties of water clouds. *J. Atmos. Sci.,* **46,** 1419–1427.

Slingo, J. M., 1987: The development and verification of a cloud prediction scheme for the ECMWF model. *Quart. J. Roy. Meteor. Soc.,* **113,** 899–927.

Smagorinsky, J., S. Manabe, and J. L. Holloway Jr., 1965: Numerical results from a nine-level general circulation model of the atmosphere. *Mon. Wea. Rev.,* **93,** 727–768.

Smith, R. N. B., 1990: A scheme for predicting layer clouds and their water content in a general circulation model. *Quart. J. Roy. Meteor. Soc.,* **116,** 436–460.

Somerville, R. C., and L. A. Remer, 1984: Cloud optical thickness feedbacks in the CO_2 climate problem. *J. Geophys. Res.,* **89,** 9668–9672.

Sundqvist, H., 1988: Parameterization of condensation and associated clouds in models for weather prediction and general circulation simulation. *Physically Based Modelling and Simulation of Climate and Climatic Change,* M. E. Schlesinger, Ed., Vol. 1, Kluwer Academic Publishers, 433–461.

——, 1993: Inclusion of ice-phase of hydrometeors in cloud parameterizations for mesoscale and large-scale models. *Contrib. Atmos. Phys.,* **66,** 137–147.

Tiedtke, M., 1993: Representation of clouds in large-scale models. *Mon. Wea. Rev.,* **121,** 3040–3061.